Erosion Quantification in Runoff Agriculture Plots by Multitemporal High-Resolution UAS Digital Photogrammetry

Sergio Arriola-Valverde, *Student Member, IEEE*, Luis Carlos Villalobos-Avellán, Karolina Villagra-Mendoza, and Renato Rimolo-Donadio, *Senior Member, IEEE*

***Abstract*—In this work, we apply close-range photogrammetry with unmanned aircraft systems to quantify erosion with millimetric spatial resolution in agricultural plots. We evaluate the proposed methodology against the traditional runoff method on active plots. A database of digital elevation models was constructed with a ground sampling distance of 7 mm/pixel and maximum root-mean-square total error of 4.8 mm, which allowed the follow-up of soil erosion dynamics within the runoff plots for a period of three months. Good agreement of the photogrammetric estimations with respect to field measurements was observed, whereas it provides a more detailed spatial information that can be used for precise soil loss dynamic studies.**

***Index Terms*—DEMs of difference (DoD), digital elevation model (DEM), photogrammetry, runoff plots, soil erosion, unmanned aerial systems (UAS).**

I. Introduction

SOIL erosion is one of the main forms of land degradation and according to recent estimations about 25% of the world-wide arable land is degraded [1]. Soil erosion is the accelerated loss of the arable layer due to the transportation of the soil particles to other sites [2] and it is a product of a combination of the erosive potential of the rainfall, vegetation cover, topography, and soil texture; it is highly related to crop productivity, food security [3], [4], and to the generation of floods in lowlands [5], [6].

Since soil erosion is highly variable in time and space, its accurate estimation becomes a challenge [2]. Many methods have been developed to quantify soil erosion; however, most of them are conducted at small scale and further extrapolated to a larger scale. For example, there are volumetric methods (rills, gullies), erosion pins, contour geotextiles for sediment retention, laser scanning, and most commonly, runoff plot methods [7]–[9]. Overall, these field methods have uncertainties on data acquisition, might not be sensitive enough to site changes, and do not represent natural runoff patterns. In addition, logistics and access to test sites for data collection might be challenging. Several authors indicate that despite runoff plots are widely used, they are ineffective and often lead to misleading results [7], [10]. Additionally, they have intrinsic high costs in construction and operation.

Alternatively, numerical models with different data input requirements and resolution have been developed for erosion quantification. The universal soil loss equation (USLE) and its revised version RUSLE [11] are empirical models developed to predict mean annual soil-loss by multiplying values of factors like rainfall-runoff erosivity, soil erodibility, topography, cover-management, and management-practices. Despite these models are often simplistic and provide gross erosion rates instead of net erosion rates [12], they are widely used [13], [14]. Other physically based mathematical models, which represent better the erosion processes at different spatial and temporal scales [12], have been developed, such as those in the Watershed Erosion Prediction Project (WEPP) [15], [16], the European Soil Erosion Model [17], the Kinematic Runoff and Erosion Model [18], the Chemical, Runoff, and Erosion from Agricultural Management Systems [19], and the Areal Nonpoint Source Watershed Environment Response Simulation [20]; their disadvantage is that they require many high spatial and temporal resolution input parameters (e.g., hydrological, topographic, vegetation, and even chemical parameters) at a large scale [12], which turns very difficult and expensive to measure over long periods of time, in particular for developing countries.

More recently, photogrammetry techniques have evolved through the utilization of computer vision methods [21], [22]. Through them, high-resolution 3-D and 2.5-D models can be created from image bundles with a wide range of image sensors, from relatively low-cost cameras up to highly specialized multi- and hyperspectral cameras [23], [24]. The image acquisition process assisted with unmanned aircraft systems (UAS) is depicted in Fig. 1.

Previous work available in the literature reports the utilization of photogrammetry for soil conservation assessment, especially when topography makes data acquisition inaccessible [25], [26],

Manuscript received June 29, 2020; revised August 24, 2020 and September 15, 2020; accepted September 23, 2020. Date of publication September 30, 2020; date of current version November 2, 2020. This work was supported by the "Vicerrectoría de Investigación y Extensión" at ITCR under the project entitled "Cuantificación de la erosión hídrica en función de diferentes técnicas de mecanización mediante vehículos aéreos no tripulados en la parte alta de la Cuenca del Río Reventazón." *(Corresponding author: Renato Rimolo-Donadio.)*

Sergio Arriola-Valverde and Renato Rimolo-Donadio are with UAS Remote Sensing and Photogrammetry Laboratory, Electronics Engineering Department, Instituto Tecnológico de Costa Rica, Cartago 30101, Costa Rica (e-mail: sarriola@tec.ac.cr; rrimolo@tec.ac.cr).

Luis Carlos Villalobos-Avellán and Karolina Villagra-Mendoza are with Agricultural Engineering Department, Instituto Tecnológico de Costa Rica, Cartago 30101, Costa Rica (e-mail: lvillaave@estudiantec.cr; kvillagra@tec.ac.cr).

Digital Object Identifier 10.1109/JSTARS.2020.3027880

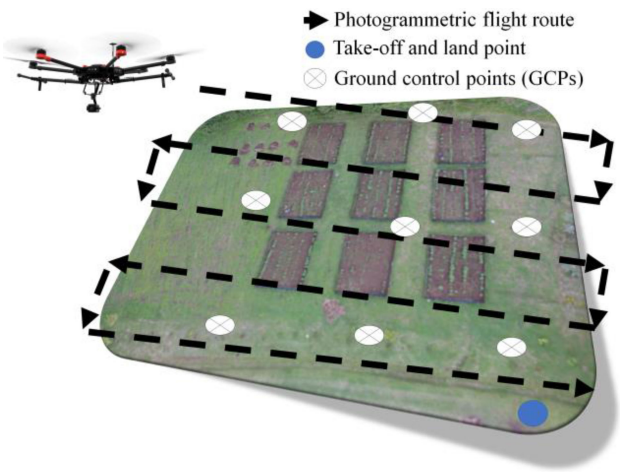

Fig. 1. Illustration of the process of a UAS photogrammetric survey over runoff agricultural plots. The plot is representative of this work, where the takeoff/land point, general flight trajectory, and ground control points are depicted.

or when the analysis on vast extensions is required to understand surface soil degradation [27], [28]. Photogrammetry has been applied mostly for soil erosion studies at large scale with resolutions starting from a few cm/pixel [29]–[32]. Some works report laboratory scale trials with millimetric resolutions [33]–[36], and a few articles report subcentimetric resolutions for coastal analysis [37] and geomorphological studies [38].

The main contributions of this work are: 1) the proposal of a close-range UAS photogrammetric methodology for the quantification of erosion in agricultural plots with resolutions below 1 cm/pixel, and 2) its quantitative evaluation against the traditional runoff method and RUSLE model on active plots. We demonstrate that UAS photogrammetry is a viable alternative to the runoff method during early crop cycles, which can provide more detailed information on soil dynamics. We show how land surface dynamics can be evaluated from a digital elevation model (DEM) database over short periods of time, in combination with the DEMs of difference (DoD) technique, proper filtering of the models and removal of vegetation coverage through an automated workflow based on the R programming language. With this approach, we compute sediment yield or loss over time, analyze soil dynamics, and compare these estimations with other field methods or mathematical models.

The rest of the article is organized as follows. In Section II, we describe the proposed photogrammetric methodology used for data collection, processing, and quantification of soil erosion. In Section III, we present a case study in Costa Rica, where the proposed methodology is applied and evaluated with respect to field measurements in runoff plots and the RUSLE model, and in Section IV, the obtained results are analyzed and discussed. Finally, in Section V, we gather the main conclusions and perspectives for further work.

II. Proposed UAS Photogrammetric Methodology

In this section, we propose a close-range UAS photogrammetry framework to analyze sediment transport and surface dynamics over agricultural plots treated with different types of soil tillage, which is later evaluated against a runoff plot method and a RUSLE model.

The UAS photogrammetry workflow consists of three main stages: aerial data acquisition, image processing, and postprocessing of photogrammetric products. Each stage is explained in the next subsections.

A. Aerial Data Acquisition

As depicted in Fig. 1, we performed the georeferenced image acquisition by setting an autonomous flight plan to cover the area under study at the lowest safe altitude and considering frontal and side image overlaps of 80%.

We selected, for this work, a Red/Green/Blue (RGB) Zenmuse-X5 sensor onboard of a medium-scale multirotor DJI Matrice 600. The RGB sensor was a CMOS (4/3) with an active area of size 17.3 $\times$ 13.0 mm. The image resolution was set to 16 megapixels (4608 $\times$ 3456 pixels), using a roller shutting technique for image forming. The optical lens was a DJI MFT of 15 mm (30 mm equivalent in 35 mm film) with a field of view of 72° and aperture range from f/1.4 to f/16.

Since we targeted the highest possible resolution, the flight height was set to 30 m due to the presence of trees and power lines nearby, which in combination with the camera parameters, allowed us to compute an estimated ground sampling distance (GSD) in cm/pixel by the following relation:

$$\text{GSD} = \frac{100 \cdot S \cdot h}{f_l \cdot I_w} \tag{1}$$

where h represents the flight height in meters, f_l is the focal length of the image sensor in millimeters, I_w corresponds to the sensor resolution in pixels, and S is the image sensor width in millimeters. The estimated ground sampling distance was of 7.5 mm/pixel.

To ensure consistency of the photogrammetric surveys over time, we installed nine ground control points (GCPs) on the experimental field that were defined and checked several times along the observation period. The GCPs were visible in the images through the utilization of acrylic black markers and white crosses with sizes of about 30 $\times$ 30 cm. We also used the GCPs to estimate spatial errors for every DEM taken over the timeline of the experiment. Although the utilization of check points is a good practice and should be used whenever possible [39], organic farming guidelines in the test site limited the number of landmarks used due to soil contamination concerns with cement and other materials required for their installation.

B. Image Processing

Each set of images collected was processed using a digital photogrammetry workflow based on Structure from Motion (SfM) and Scale-Invariant Feature Transform algorithms [22], [40], implemented in the commercial software tool *Agisoft Metashape*, version 1.5.5.

We used a limit of 40 000 key points and 4000 tie points for the alignment and construction of the sparse point cloud, followed by a noise filtering stage with the gradual selection method [41].

The Costa Rica's projection system CRTM05/CR05 [42] was used for the alignment and organization of the image bundle. GCPs were inserted as markers and used to provide a precise geospatial localization to all photogrammetric models.

We used the full resolution image bundle with the multiview stereo approach provided by *Agisoft Metashape* to form the dense point cloud with the highest possible resolution. From there, we computed the mesh model through a triangulated irregular network interpolation and the DEM with another interpolation method called inverse distance weighting.

The root-mean-square error (RMSE) was computed to evaluate the georeferencing error in the GCPs, as it will be shown in the next section. The output of this image processing workflow was the database of DEMs and orthomosaics corresponding to each observation time.

C. Postprocessing of Information

We exported DEMs and orthomosaics in a raster format to select the areas of interest within a geographic information system environment such as QGIS version 3.14.0. The GSD was equalized in all database entries, considering a GSD of 7 mm/pixel in this work, by resampling the raster models corresponding to the six observation times using a bilinear interpolation method.

We applied the DoD technique [43], where two DEMs at different epochs (i.e., observation times) were pixel-wise subtracted to analyze soil dynamics and to quantify soil accumulation or loss. In order to filter noise and outliers in the DoDs, we used an RMSE propagation method for establishing a Level of Detection (LoD) that indicates the minimum vertical difference that can be considered to be beyond the uncertainty range of the models [43]. The vertical LoD was computed by the root square addition of the RMSE values associated with the two epochs used to calculate the DoD, identified with the subindex *i* and *j*, according to

$$\mathrm{LoD}_z = \sqrt{\left(\mathrm{RMSE}_{\mathrm{DEM}_i}\right)^2 + \left(\mathrm{RMSE}_{\mathrm{DEM}_j}\right)^2}. \quad (2)$$

We incorporated two filtering approaches to remove the noise floor and the vegetation coverage from the calculations. The first filtering stage suppressed the values below the ±LoD. The second filtering stage was performed by constructing a binary mask *I(x, y)* designed to remove vegetation by defining an upper and lower difference threshold that cannot be associated with soil variations, defined by

$$I_{(x,y)} = \begin{cases} 1 & -\text{Threshold} < I_{(x,y)} < +\text{Threshold}, \\ 0 & \text{Otherwise}. \end{cases} \quad (3)$$

Through this mask it was possible to reclassify DoD pixels associated with values of "1" in the mask as soil, and "0" values as vegetation.

The evaluation of the spatial elevation changes over time was carried out through the QGIS profile tool. Soil loss was determined from the filtered DoD, by performing a pixel raster sum to estimate the total amount of eroded and deposited soil.

Since the process described before is highly repetitive, applied on all pixels and combination of DEMs in raster format at different epochs, these tasks were automated by scripting with the R statistical suite v.4.0.2 using R-Studio v.1.3.1.

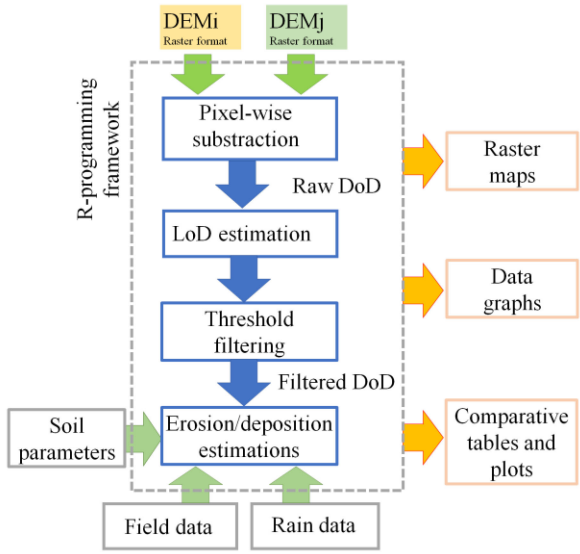

Fig. 2. Schematic representation of the proposed R-programming framework functionalities, inputs, and outputs for automation of the postprocessing of DEMs for two arbitrary observation epochs *i* and *j*.

Fig. 2 depicts the tasks performed by the R-scripts, inputs, and the generated outputs, which are derived from two raster DEMs covering the area of interest: DoD computation, LoD estimation and filtering, threshold filtering to remove vegetation coverage (and any other element not associated with soil surface), and net loss computations. This process can be iteratively applied between arbitrary epochs and allows the automatic computation and generation of results in a convenient way.

We compared the obtained results from close-range UAS photogrammetry and the runoff plot method through the RMSE, percentage bias (PBIAS), and the determination coefficient (R^2), defined as follows:

$$\mathrm{RMSE} = \sqrt{\frac{\sum_{i=1}^{n}\left(Y_{\mathrm{observed}} - Y_{\mathrm{calculated}}\right)^2}{n}}, \quad (4)$$

$$\mathrm{PBIAS} = \left(\frac{\sum_{i=1}^{n}\left(Y_{\mathrm{observed}} - Y_{\mathrm{calculated}}\right)}{\sum_{i=1}^{n}\left(Y_{\mathrm{calculated}}\right)}\right) \cdot 100, \quad (5)$$

$$R^2 = \frac{\mathrm{cov}^2\left(Y_{\mathrm{observed}}, Y_{\mathrm{calculated}}\right)}{var\left(Y_{\mathrm{observed}}\right) var\left(Y_{\mathrm{calculated}}\right)} \quad (6)$$

where Y_{observed} represents the amount of collected sediment in the field and $Y_{\mathrm{calculated}}$ is the calculated sediment from the photogrammetric analysis, with n as the number of observations. The smaller the RMSE value the better the model accuracy, and results with RMSE values below half of the standard deviation of the collected sediments were considered as an acceptable model estimation [44]. PBIAS values were used to evaluate the relative difference between collected and estimated sediments, where a negative value means an underprediction and a positive value indicates an overprediction. The correlation coefficient (R) was used to estimate the trend in the correlation of the collected and estimated observations [45], [46].

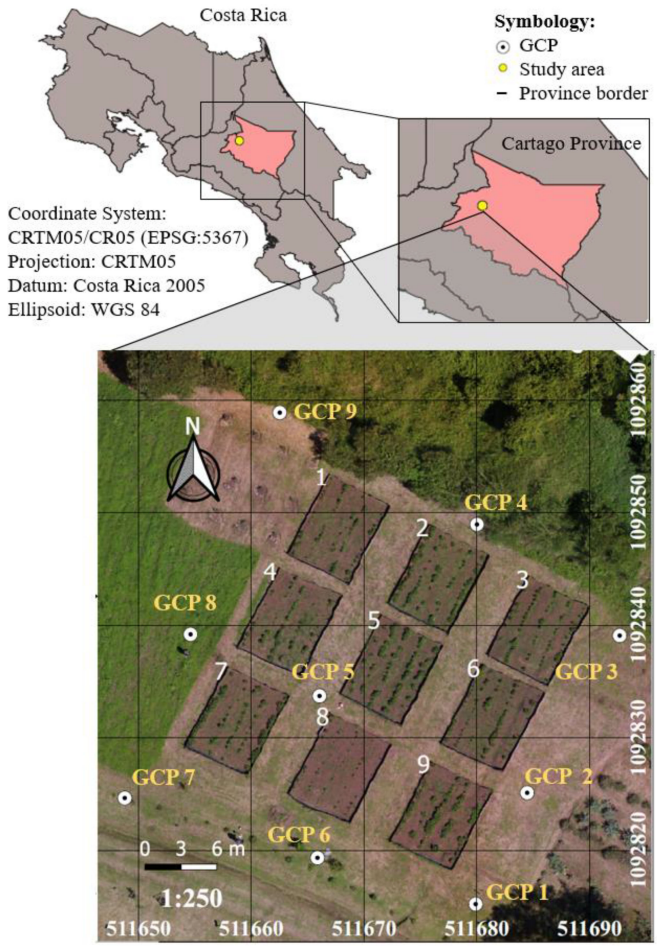

Fig. 3. Location map of the experimental agriculture plots at INA, La Chinchilla, Cartago, Costa Rica. The nine runoff plots, their numbering, and the GCPs are shown in the map.

III. Case Study

We discuss in this section a case study in Cartago, Costa Rica, where the UAS photogrammetric methodology was applied. The aim of this study is to quantitatively compare the effectiveness of the proposed UAS photogrammetric approach against the runoff plot method, analyze advantages and disadvantages, and to correlate the obtained results by each method. The results are also discussed taking into consideration the estimations obtained through the RUSLE model.

The study was conducted at the Center of Organic Agriculture, La Chinchilla, of the Instituto Nacional de Aprendizaje (INA), at a latitude of 9.883304 and a longitude of –83.893587 (WGS 84 coordinate system), equivalent to 1092840 N and 511670 E in the local CRTM05 projection system, and an altitude of 1613 m above the sea level. The climate of this subregion, called West Central Valley (VC2), belongs to the humid low montane forest and the average annual temperature varies between 12 and 17 °C; the average annual precipitation is 2016 mm, which concentrates during the rainy reason from May to November [47]. Soils are predominantly Andosol types with clay texture [47]. The slope was 16%, with a north-west to south-east orientation, and the vegetation coverage was mainly formed by grass and short-cycle low density crops. We installed nine runoff plots that were cultivated with black bean seeds, planted in rows parallel to the slope direction (see Fig. 3).

TABLE I
Characteristics of Experimental Plots

Characteristic	Runoff plot		
	P4	P5	P8
Area, m^2	49.48	48.45	48.71
Slope, %	15.82	16.54	13.05
Soil type	Clay	Clay	Clay
ρ_d, g/cm^3	0.99	1.1	1.04
Ib, mm/h	0.0028	0.0107	0.0241
Plow depth, cm	23	30.5	18

Note: ρ_d: bulk density, Ib: final infiltration rate.

A. Field Data Collection

Nine runoff plots with an average area of 48 m^2 (8 m long $\times$ 6 m wide) were installed in a field used for crop production. Each runoff plot area was delimited by metallic sheets inserted into the soil at the top and at the lateral sides. At the bottom, a geotextile was installed to retain sediments and simultaneously allowing water to pass through.

A rain gauge with data logger, model TR-525USW with a maximum resolution of 0.2 mm, was installed on site to register rainfall intensities every 5 min during the observation period. Soil sediments deposited at the bottom of each plot, over the geotextile, were collected in bags, labeled, and transported to the laboratory for sample processing on a weekly basis. Fresh sediments, from each runoff plot, were weighed and then oven-dried at 105 °C for 24 h. The amount of soil loss in each runoff plot was determined by the oven dry weight.

Additionally, we computed physical soil properties of the area under study (see Table I). Soil texture was determined with the hydrometer method, combined with a sieve analysis (0.063–2 mm) [48] and the classification was based on FAO guidelines [49]. Undisturbed soil samples were obtained at a depth of 15 cm, with cylinders of ca. 100 cm^3. Bulk density (ρ_d) was determined by dividing the oven-dry weight of an undisturbed soil sample by its volume. Final infiltration rate (I_b) was determined using a mini disk infiltrometer model S by METER Group.

B. UAS Photogrammetric Approach

The photogrammetric flights were performed, with a periodicity from one to two weeks, from September 11 to November 6, 2018. Observation intervals were dependent on weather conditions. The autonomous missions were configured through the software application DJI GS PRO, with the parameters mentioned before: front and side overlaps of 80%, flight height of 30 m, and an estimated GSD of 7.5 mm/pixel. About 90 photos per mission were taken, and the RGB camera sensor was configured with an ISO value of 100, f-number ranges from 1.7 to 2.5, and shutter speed ranges from 1/3200 to 1/8000 s. The parameters were fixed for each survey, varying within different observation times due to light conditions.

TABLE II
GCP COORDINATES IN THE CRTM05 PROJECTION SYSTEM

GCP ID	North (N) (m)	East (E) (m)	Elevation (Z) (m)
1	1092815.2120	511679.8950	1612.2490
2	1092825.1040	511684.4620	1613.7350
3	1092839.0730	511692.6660	1616.5540
4	1092848.9480	511680.0080	1617.1720
5	1092833.7080	511666.0450	1613.6310
6	1092819.3250	511665.8620	1611.7700
7	1092824.6380	511648.7680	1611.7590
8	1092839.1840	511654.6060	1613.9040
9	1092858.8820	511662.5180	1617.4920

TABLE III
AVERAGE X/Y/Z COORDINATE AND TOTAL RMSE PER EPOCH

Epoch number	Epoch*	$RMSE_X$ (mm)	$RMSE_Y$ (mm)	$RMSE_Z$ (mm)	$RMSE_{total}$ (mm)
1	Sep. 11	3.9476	2.6771	0.4493	4.7696
2	Sep. 25	1.0369	0.6013	0.2810	1.1986
3	Oct. 2	1.5958	0.9882	0.4022	1.9196
4	Oct. 9	0.4919	0.9671	0.1936	1.1021
5	Oct. 23	1.8250	2.1539	1.2575	3.0905
6	Nov. 6	0.9975	1.3945	0.8896	1.9315

Note: *Dates correspond to year 2018.

TABLE IV
MAXIMUM GCP SPATIAL ERROR PER EPOCH

Epoch number	Epoch*	GCP ID†	X Max. error (mm)	Y Max. error (mm)	Z Max. error (mm)
1	Sep. 11	5	8.0	-4.0	1.0
2	Sep. 25	2	3.0	0.0	1.0
3	Oct. 2	6	3.0	-1.0	0.0
4	Oct. 9	2	-1.0	3.0	1.0
5	Oct. 23	8	-1.0	5.0	-1.0
6	Nov. 6	8	2.0	3.0	-1.0

Note: *Dates correspond to year 2018.
†GCP ID showing the maximum spatial error extracted from projected CRTM05 coordinates.

TABLE V
GSD VALUES IN DIGITAL ELEVATION MODELS

Epoch number	Epoch*	$GSD_{Estimated}$ (mm/pixel)	$GSD_{Obtained}$ (mm/pixel)	Difference (%)
1	Sep. 11	7.50	7.43	0.93
2	Sep. 25	7.50	7.27	3.07
3	Oct. 2	7.50	7.36	1.87
4	Oct. 9	7.50	7.46	0.53
5	Oct. 23	7.50	7.38	1.60
6	Nov. 6	7.50	7.40	1.33

Note: *Dates correspond to year 2018.

TABLE VI
ERROR PROPAGATION FROM VERTICAL RMSE VALUES

DoD Epochs	$RMSE_{t_{n+1}}$ (mm)	$RMSE_{t_n}$ (mm)	LoD (mm)
Sep. 25 – Sep. 11	0.2810	0.4493	0.5299
Oct. 2 – Sep. 25	0.4022	0.2810	0.4906
Oct. 9 – Oct. 2	0.1936	0.4022	0.4464
Oct. 23 – Oct. 9	1.2575	0.1936	1.2723
Nov. 6 – Oct. 23	0.8896	1.2575	1.5404
Nov. 6 – Sep. 11*	0.8896	0.4493	0.9966

Note: *Last DoD epoch corresponds to the difference of DEMs between the last and first epoch of the observation period.

The nine GCPs (illustrated in Fig. 3 and defined in Table II) were georeferenced with a Leica GS-14 L1/L2 GNSS-RTK station, using a base landmark point with millimetric resolution, located 10 km away from the study site at the Instituto Tecnológico de Costa Rica, Cartago Campus. The hold time for the base point was about 2 h. Each point was taken in postprocessing mode with a hold time of 10 min and a minimum of 12 GPS/GLONASS satellites. Considering that the survey area is relatively small, this hold time was determined by iterative trials.

The processing of image bundles per epoch was performed on a workstation with 2 Xeon multicore processors at 2.5 GHz with 32 threads, 64 GB of RAM memory and an Nvidia Quadro GPU with 4 GB of RAM. The gradual selection filtering of the sparse point cloud in *Agisoft Metashape* was performed with the following parameters: reprojection error below 0.12, reconstruction uncertainty below 15, and projection accuracy below 2. With this, total RMSE values could be maintained below 4.8 mm in the georeferencing, as shown in Table III for the different epochs.

Table IV shows the maximum spatial errors that were registered for any GCP per epoch, calculated as the difference between the measured and calculated coordinate values in the CRTM05 projection system; it can be observed that the maximum error (8 mm) is in the same order of magnitude with respect to the GSD.

For the dense point cloud generation, a computing time of about 20 h per image set was required using full image resolution (ultrahigh quality and depth filtering setting). Obtained GSD values were slightly better in all cases with respect to the estimated value of 7.5 mm (see Table V). As mentioned before, all the obtained DEMs were resampled with the bilinear interpolation to have a uniform GSD of 7 mm/pixel.

Finally, the DoD technique was applied to the DEM database. Through the R-programming framework, any possible combination of observation points can be computed. Table VI shows the results of the error propagation analysis for a subset of DoDs, with vertical LoD levels below 1.6 mm.

Since any kind of pesticide was not allowed at the INA La Chinchilla, undergrowth was manually controlled; nevertheless, the filtering had to be customized for each observation point due to variability of the vegetation coverage along the observation times.

In this article, a subset of results will be discussed, related to plots 4, 5, and 8. Runoff plot 4 was tilled with chisel plow (P4), runoff plot 5 with spading machine (P5), and runoff plot 8 with power harrow (P8).

In Table VII, we show the calculated upper and lower threshold values that define the range interpreted as soil when the DoD is filtered. Fig. 4 shows an example with two orthomosaic views of runoff plot 5 at the first and last epochs, the resulting DoD with

TABLE VII
THRESHOLD VALUES USED TO FILTER VEGETATION COVERAGE

Plot	DoD Epoch	Lower Value (cm)	Upper Value (cm)
P4	Sep. 25 – Sep. 11	-5.30	4.00
	Oct. 2 – Sep. 25	-3.75	3.30
	Oct. 9 – Oct. 2	-4.67	3.50
	Oct. 23 – Oct. 9	-4.75	3.75
	Nov. 6 – Oct. 23	-3.00	1.80
	Nov. 6 – Sep. 11	-7.25	3.50
P5	Sep. 25 – Sep. 11	-5.00	3.50
	Oct. 2 – Sep. 25	-6.00	3.50
	Oct. 9 – Oct. 2	-4.50	4.35
	Oct. 23 – Oct. 9	-7.25	2.00
	Nov. 6 – Oct. 23	-5.20	2.00
	Nov. 6 – Sep. 11	-10.9	3.00
P8	Sep. 25 – Sep. 11	-4.00	3.40
	Oct. 2 – Sep. 25	-5.50	5.25
	Oct. 9 – Oct. 2	-6.00	5.85
	Oct. 23 – Oct. 9	-10.05	2.00
	Nov. 6 – Oct. 23	-3.00	2.50
	Nov. 6 – Sep. 11	-10.90	3.00

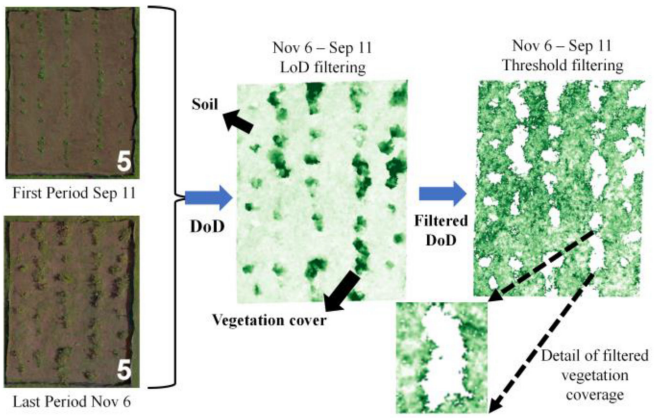

Fig. 4. Example of filtered DoD for runoff plot 5. (a) Orthomosaic views for the first (September 11) and last (November 6) epochs. (b) DoD with LoD filter applied. (c) DoD with threshold filter applied. A threshold range from –10.9 to 3 cm was used to obtain the final DoD.

the LoD filter, and the final DoD with the threshold (vegetation) filter applied.

C. RUSLE Model

The collected sediments and estimations by the photogrammetric approach were also compared with the soil loss predicted by the empirical soil erosion model RUSLE [11]. The required model input parameters to estimate the gross soil erosion for each epoch are rainfall-runoff erosivity *factor, soil erodibility factor, slope length factor, slope steepness factor, cover-management factor, and support practice factor*.

The *rainfall-runoff erosivity* (*R*) was calculated according to the following equation:

$$R = \frac{\sum_{k=1}^{n} (E_c \cdot I_{30})_k}{N} \tag{7}$$

TABLE VIII
SOIL INPUT PARAMETERS OF THE RUSLE MODEL

Input parameter	Runoff plot		
	P4	P5	P8
MO, %		1.61	
M, %		1604.06	
Structure (s)		blocky	
Permeability (p)		moderate	
% clay		55.75	
% silt		26.25	
% sand		8.00	
% fs		10.00	
X, m	5.93	5.92	5.95
m, (-)	0.58	0.59	0.56

Note: %fs:fine sand (0.05–0.1 mm), % silt: 0.002–0.05 mm, % sand: 0.1–2 mm.
s:1—very fine granular, 2—fine granular, 3—med or coarse granular, 4—blocky, platy, or massive.
p: 1-rapid, 2-med to rapid, 3-moderate, 4-slow to med, 5-slow, 6-very slow.

where n is the number of storms in an N week period. The I_{30} component is the maximum consecutive 30-min intensity (mm/h) for a given storm. The storm energy, E_c, component (MJ/ha) was determined by the following fitting equation:

$$E_c = [0.29 \cdot (1 - 0.72 \exp(-0.05 \cdot I_N))] \cdot P_N. \tag{8}$$

where I_N (mm/h) and P_N (mm) are the intensity and amount of precipitation for the recorded storm interval, respectively.

The *soil erodibility factor* (*K*) was calculated by

$$K = \frac{2.1 \cdot 10^{-4} \cdot (12 - M_0) \cdot M^{1.14} + 3.25 \cdot (s-2) + 2.5 \cdot (p-3)}{100}. \tag{9}$$

Here, M_0 corresponds to soil organic matter (in %), M is the product of the primary particle size fractions: (% of soil size fractions between 0.002 and 0.1 mm)·(% of silt + % of sand), s corresponds to the classes for soil structure, and p is the class corresponding to soil permeability. The factor *K* was divided by 7.59 to convert it to SI units of ton-ha-h/(ha-MJ-mm).

The *slope length factor* (*L*) was determined by

$$L = \frac{(X)^m}{22.1} \tag{10}$$

where X is the horizontal projection of the slope length (in meters), 22.1 is the RUSLE unit plot length (in meters), and m is the slope-length exponent related to the ratio of rill erosion to interrill erosion, represented by the following equation:

$$m = \frac{\text{sen}\theta}{\text{sen}\theta + 0.269(\text{sen}\theta)^{0.8} + 0.05} \tag{11}$$

with θ being the slope angle (in degrees).

The *slope steepness factor* (*S*) was evaluated by

$$S = 16.8\,\text{sen}\theta - 0.50, \text{ for slope } \geq 9\%. \tag{12}$$

Cover-management (*C*) and *support practice* (*P*) factors were set to 1, since the runoff plots were managed under clean tilled fallow conditions without the utilization of a specific conservation practice. The input parameters are gathered in Table VIII.

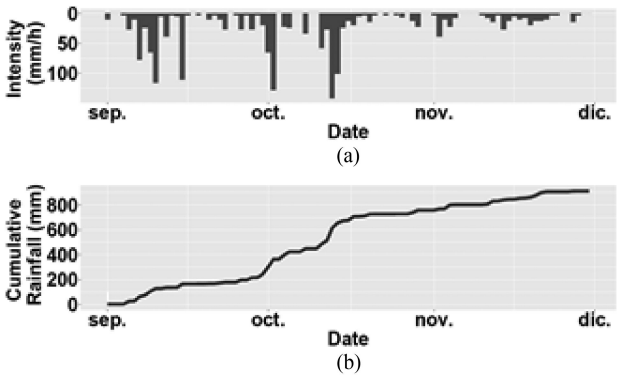

Fig. 5. Rainfall events from September to November 2018, registered at the test site. (a) Hyetogram of the rain intensity in 5 min. (b) Daily cumulative rainfall during the observation period.

TABLE IX
PRECIPITATION PER MONTH DURING THE OBSERVATION PERIOD

Period	Daily average (mm)	Standard deviation (mm)	I_{30} (mm/h)
September	8.17	11.16	110.0
October	16.57	24.18	108.8
November	5.06	7.97	14.2

As shown in Fig. 5, important rainfall events occurred mostly during the period from mid-September to mid-October, with a maximum 5 min rainfall intensity of 141.60 mm/h in October 13. The highest average daily precipitation was also registered in October, with a value of 16.57 mm. Table IX summarizes the rainfall averages, standard deviations, and the maximum 30 min intensity (I_{30}) registered per month, which will be used in the next section to correlate the soil loss estimations.

IV. RESULTS AND DISCUSSION

Table X shows the estimated cumulative sediments in the experimental runoff plots P4, P5, and P8, obtained by close-range photogrammetric analysis, by manual field collection, and by the RUSLE model. We observed similar trends and good agreement regarding cumulative sediments over the observation period, except for predictions by the RUSLE equation (as it will be discussed next).

In runoff plot P4, the photogrammetric analysis predicted cumulative changes with respect to previous DoD epochs of 26%, 62%, 34%, and 17%, respectively, compared to 23%, 61%, 39%, and 16% reported by manual onsite collection; in runoff plot P5, photogrammetric changes accounted for 186%, 4%, 128%, and 27%, compared to 195%, 0%, 130%, and 29% reported on-site; and lastly, in runoff plot P8 the same comparison yielded cumulative changes of 59%, 25%, 1105%, and 3%, versus 51%, 0%, 1452%, and 3%, respectively.

No changes reported on cumulative sediment in the manual collection method were due to limitations to gather little amounts of sediments deposited on the geotextile. In contrast, with close-range UAS photogrammetry, we were able to detect small land surface changes in the centimetric range.

The highest amount of sediments was registered, with all methods, in the time range from October 9 to October 23, as a result of the high rainfall intensity recorded (see Fig. 5) and probably due to the high soil moisture content produced from the consecutive rainfall events observed during this month.

Soil erosion was expected to occur in all runoff plots, since the type of soil in the test site is highly associated with low infiltration rates (see Table I) [50], which facilitates surface runoff and consequently soil erosion.

The RUSLE model estimated, in average, three times more sediment than the manual field collection. These differences are part of the intrinsic limitations of the RUSLE model, since it depends on empirical parameters, only predicts the gross erosion, and does not account for the deposition that might occur in the field [12]. Therefore, it tends to overestimate erosion rates, particularly for small areas and short periods of time. Although its simplicity makes this model the most common used tool, it lacks connection to the sediment transport processes. For example, Wang *et al.* [51] tested the performance of RUSLE, in south China, with unsatisfactory results since it was not able to accurately reproduce the effect of steep slopes and complex topography. In Brazil, Amorim *et al.* [52] compared soil loss estimations of WEPP, USLE, and RUSLE with respect to field soil loss measurements and obtained a soil loss estimation accuracy of 46% with the WEPP model, 42% with RUSLE, and 12% with USLE. Efthimiou *et al.* [53] tested the performance of RUSLE in the Mediterranean, obtaining inconsistency in the annual soil loss estimations in different catchments due to limitations of the model representing specific characteristics of the study area.

Soil loss differences observed among the reported plots in sediment estimations can be attributed to the tillage techniques used. Runoff plot P5 (spading machine) registered the highest amount of sediments during this study, followed by P8 (power harrow).

Normally, subsoil compaction is caused by the tillage system and the plow pan formed at the plow depth is considered as an indicator of subsoil compaction [54]. In this case, the plow pan in P8 (power harrow) was closer to the surface, promoting the cumulation of excess water at the surface; however, because the slope was smaller than P4 and P5, soil deposition could have occurred before reaching the bottom levels of the plot.

Here, the RUSLE model was not able to estimate soil loss changes due to the different tillage systems (spading machine, power harrow, or chisel), which are not identified in the support practice factor (P). The P-factor considers conservation practices such as contouring, strip cropping, and terracing, but it is not sensitive to any tillage system. The detailed discussion on the influence of tillage procedures on erosion will be discussed in future works.

Since the runoff plot method and photogrammetric approaches provided similar and more accurate results, further result comparisons were performed for these methods only. Table XI shows the overall computed PBIAS, RMSE, and R^2 parameters between these two approaches, described in (4)–(6) for each of the three evaluated plots. The UAS photogrammetric approach correlates well with soil loss with respect to field measurements. The PBIAS parameter showed that the

TABLE X
CUMULATIVE SEDIMENT ESTIMATED AND COLLECTED FROM SEPTEMBER TO NOVEMBER 2018

DoD Epochs	Daily Cumulative rainfall (mm) **	Cumulative sediment estimated by UAS Photogrammetry (g)			Cumulative sediment manually collected in the runoff plots (g)			Gross soil erosion estimation with RUSLE model (g)		
		Plot 4	Plot 5	Plot 8	Plot 4	Plot 5	Plot 8	Plot 4	Plot 5	Plot 8
Sep. 25 – Sep. 11	50	241.4	281.6	87.0	241.2	261.8	89.7	658.0	673.9	529.6
Oct. 2 – Sep. 25	235	304.7	806.3	138.7	297.2	773.4	135.7	835.0	855.2	672.1
Oct. 9 – Oct. 2	321	494.9	834.9	172.8	478.6	773.4*	135.7*	2607.6	2670.6	2098.7
Oct. 23 – Oct. 9	599	664.1	1905.8	2082.1	663.2	1776.3	2106.1	3966.8	4062.7	3192.6
Nov. 6 – Oct. 23	673	778.1	2413.5	2136.1	771.6	2285.0	2162.9	4008.1	4105.0	3225.8

Note: *No field data collection during this week.
**Cumulative rain for the complete observation period.

TABLE XI
STATISTICAL METRICS FOR COMPARISON OF THE PHOTOGRAMMETRIC APPROACH WITH RESPECT TO THE RUNOFF PLOT METHOD

Plots	PBIAS (%)	RMSE (g)	R^2
P4	1.3	8.6	0.9992
P5	6.3	87.8	0.9997
P8	-0.3	23.2	0.9998

photogrammetric approach estimated 1.3% and 6.3% more soil loss in P4 and P5, respectively, and 0.3% less soil loss for P8 with respect to the field sediment collection. The total RMSE values were relatively small compared to the amount of collected material and the trends predicted by both methods yield an R^2 coefficient approaching to one.

The resolution of 7 mm/pixel and a total georeferencing RMSE below 4.8 mm, achieved with the UAS photogrammetric approach, are comparable to other works that report subcentimetric resolution, e.g., for coastal management in [37], and better that most works on erosion assessment that usually reports resolutions and errors of several centimeters [29].

Note that RMSE values represent average errors and are determined at the GCP locations; therefore, they provide an error expectation assuming that the number and position of GCPs are sufficient and representative of the area under study. The worst-case absolute error at certain epochs, points, and directions can be larger than the RMSE and this bound is also important to assess the accuracy of soil loss estimations; in this case, as shown in Table IV, the worst-case absolute referencing error of 8 mm is still in the same order of the pixel size and this suggests that a good degree of confidence was achieved. To take advantage of a high spatial resolution, it becomes evident that an adequate georeferencing strategy that can limit the error to small values is of utmost importance.

A general advantage of the photogrammetric approach is indeed the high temporal and spatial resolution that can be achieved and that allows the exploration of the soil dynamics in detail. Both resolutions are adjustable according to the requirements of the analysis, and multiple observations and quantitative estimations can be simultaneously performed on several test sites. In Figs. 6 and 7, we depict examples of some information that can be extracted from DEM and DoD databases.

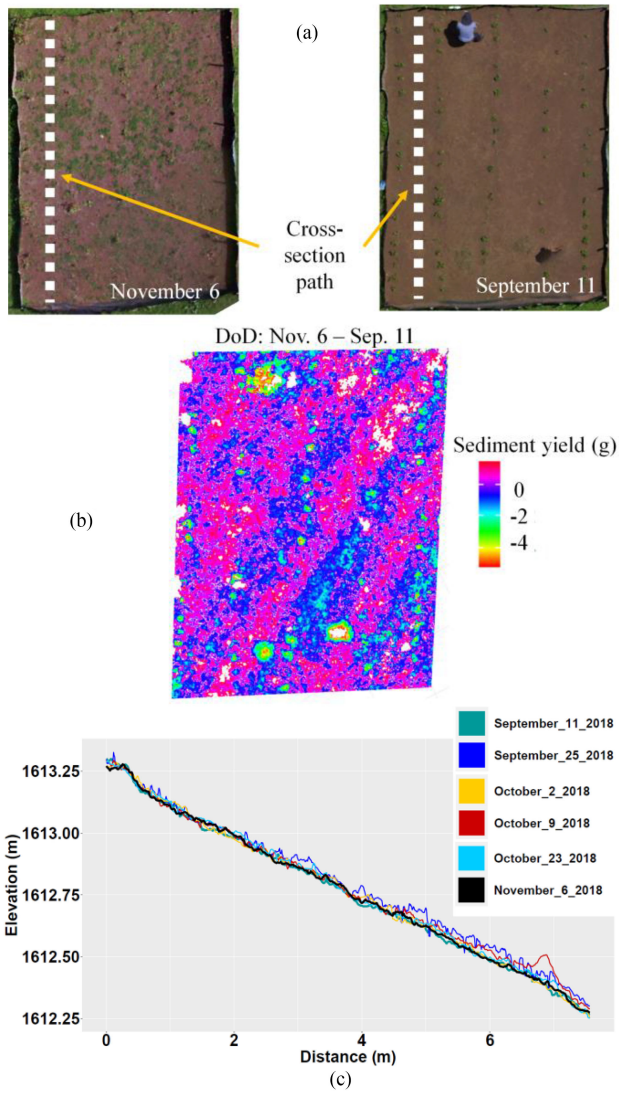

Fig. 6. Example of spatial analysis for plot P8. (a) Orthomosaic views for the first and last epochs. (b) Prefiltered DoD, and (c) terrain profile over a cross section path on DEMs for all epochs.

Fig. 6 shows the orthomosaic views at two epochs (September 11 and November 6) for plot P8. Vegetation coverage was low at these two epochs since the plants started decaying in November due to the attack of the white fly. We presented a

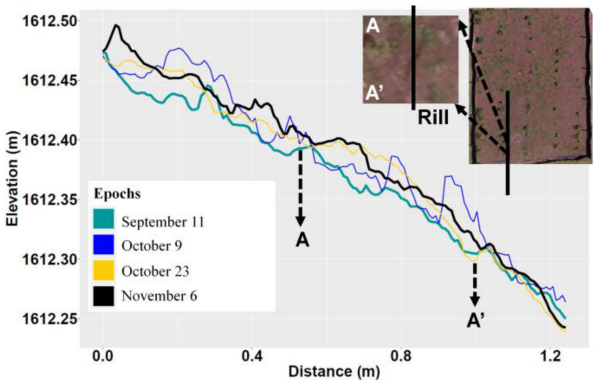

Fig. 7. Inspection of a rill formation over time from DEM cross sections. The orthomosaic view shows the detail of the rill during the peak rainfall period (October 9).

photogrammetric analysis of the biomass related to this study site in [55].

Additionally, from these orthomosaics, the unfiltered DoD is displayed. Note that the person on the top side of the initial orthomosaic in September 11 [not present in the last epoch, Fig. 6(a)] appears as a negative difference in the DoD of Fig. 6(b). Soil loss estimations require, as discussed before, filtering of the DoD to remove vegetation coverage and any other object present in the orthomosaics.

Vegetation coverage is an important challenge when applying photogrammetric techniques, and the low-density coverage typical of early crops is the ideal scenario to evaluate erosion processes; nevertheless, vegetation needs to be properly filtered to avoid errors for erosion estimations and in cases with a dense coverage, the analysis could become unfeasible.

Fig. 6(c) shows the cross-section profile of a path defined in P8 [see Fig. 6(a)]. A longitudinal polyline was defined as observation path on DEMs to analyze closely the soil surface dynamics at the different epochs. Soil surface dynamics is a function of previous surface conditions, hillslope, and rainfall intensity. Initially, soil surface was homogenous, and as different rain events occurred, sediment was transported from upside hill and deposited downward. Two extreme 5 min rainfall events of 141 and 100 mm/h occurred in two consecutive days (between October 9 and October 23), increasing soil moisture and surface runoff, which consequently eroded the previous deposited material at the bottom of the plot. By relating changes over the polylines to rainfall intensity (corresponding to the end of each epoch), we can observe that low rainfall intensity produced surface runoff with low transport capacity.

Fig. 7 depicts a case where the close-range UAS photogrammetric method enables specific analyses of the soil surface in a detailed way and with the requirement of just a few input parameters. In this case (cross section along path A-A'), erosion and deposition processes are shown during different rain events and even showing the formation of a rill during the peak rain period.

V. Conclusion and Outlook

In this work, we analyzed the utilization of close-range photogrammetry for the quantification of soil erosion with respect to the well-known method of runoff plots and the RUSLE model. It was demonstrated that the photogrammetric approach can provide accurate results in the subcentimetric range and a lot more spatial information to analyze soil dynamics, without the problems associated with the manual sampling process required by the traditional runoff method or physical parameters required by empirical models.

Overall, UAS photogrammetry constitutes a useful approach to register land surface dynamics, which can provide valuable information for decision making on soil conservation practices.

The photogrammetric approach can work well with a wide range of UAS platforms, but it requires modest computational resources and several hours of processing time; however, this is compensated by a simpler and less prone-to-error data acquisition phase in comparison to manual quantification methods. High-precision ground control points were used in this study to explore the accuracy limits, but other simpler and less expensive referencing strategies can be used when larger errors can be tolerated. The definition of the required GSD and maximal error is an important decision, since it is strictly related to the effort and cost of the deployment in the photogrammetric approach.

Future work will address the impact of tillage techniques on erosion processes and the construction of erosion models from photogrammetric products, which in combination of the utilization of other types of sensors might provide a more robust, precise, and reliable approach in contrast to methods that strongly rely on soil samples and other input parameters. For instance, the utilization of multi- or hyperspectral sensors in combination with artificial intelligence techniques may enable soil dynamics analyses together with the identification of soil parameters.

Acknowledgment

The authors would like to thank F. Pacheco-Rodriguez and the staff of the Organic Agriculture Center, INA La Chinchilla, Cartago, Costa Rica, for lending the farmland used in this study. The authors would also like to thank M. Solórzano and N. Gómez, from the Agricultural Engineering Department at ITCR, for the field data collection and processing, and to M. Méndez-Morales and B. Umaña-Quirós, from the Construction Engineer Department at ITCR, for the useful discussions and suggestions made for setting up the photogrammetric analysis and georeferencing points.

References

[1] FAO, *The State of the World's Land and Water Resources for Food and Agriculture: Managing Systems at Risk*, Food and Agriculture Organization of the United Nations, Rome and Earthscan, London, 2011, ch. 3. [Online]. Available: http://www.fao.org/3/i1688e/i1688e00.htm

[2] FAO, *Status of the World's Soil Resources (SWSR) – Main Report*. Rome, Italy: Food Agriculture Org. United Nations, 2015. [Online]. Available: http://www.fao.org/3/i5199e/i5199e.pdf, Accessed: Oct. 8, 2020.

[3] H. Kumar and P. Pani, "Effects of soil erosion on agricultural productivity in semi-arid regions: The case of Lower Chambal Valley," *J. Rural Develop.*, vol. 32, no. 2, pp. 165–180, 2012.

[4] H. Lin, Y. Xie, G. Liu, J. Zhai, and S. Li, "Soybean and maize simulation under different degrees of soil erosion," *Field Crops Res.*, vol. 230, pp. 1–10, 2019, doi: 10.1016/j.fcr.2018.10.004.

[5] Y. Lu, R. Bookman, N. Waldmann, and S. Marco, "A 45 kyr laminae record from the Dead Sea: Implications for basin erosion and floods recurrence," *Quaternary Sci. Rev.*, vol. 229, 2020, Art. no. 106143, doi: 10.1016/j.quascirev.2019.106143.

[6] J. Boardman, "Soil erosion and flooding on the Eastern South Downs, Southern England," *Trans. Inst. Brit. Geographers*, vol. 28, no. 2, pp. 176–196, 2003.

[7] Y. P. Hsieh, K. T. Grant, and G. C. Bugna, "A field method for soil erosion measurements in agricultural and natural lands," *J. Soil Water Conserv.*, vol. 64, no. 6, pp. 374–382, 2009, doi: 10.2489/jswc.64.6.374.

[8] N. Hudson, *Field Measurement of Soil Erosion and Runoff*. Rome, Italy: Food Agriculture Org. United Nations, 1993. [Online]. Available: http://www.fao.org/3/T0848E/t0848e00.htm, Accessed: Oct. 8, 2020.

[9] P. I. A. Kinnell, "A review of the design and operation of runoff and soil loss plots," *Catena*, vol. 145, pp. 257–265, 2016, doi: 10.1016/j.catena.2016.06.013.

[10] J. Boardman, "Soil erosion science: Reflections on the limitations of current approaches," *Catena*, vol. 68, nos. 2/3, pp. 73–86, 2006.

[11] K. G. Renard, G. R. Foster, G. A. Weesies, D. K. McCool, and D. C. Yoder, "Predicting soil erosion by water: A guide to conservation planning with the revised universal soil loss equation (RUSLE)," USDA, Washington, DC, USA, 1997.

[12] C. Alewell, P. Borrelli, K. Meusburger, and P. Panagos, "Using the USLE: Chances, challenges and limitations of soil erosion modeling," *Int. Soil Water Conservation Res.*, vol. 7, pp. 203–225, 2019.

[13] B. P. Ganasri and H. Ramesh, "Assessment of soil erosion by RUSLE model using remote sensing and GIS - A case study of Nethravathi Basin," *Geosci. Front.*, vol. 7, pp. 953–961, 2016, doi: 10.1016/j.gsf.2015.10.007.

[14] G. Ashiagbor, E. K. Forkuo, P. Laari, and R. Aabeyir, "Modeling soil erosion using RUSLE and GIS tools," *Int. J. Remote Sens. Geosci.*, vol. 2, no. 4, pp. 7–17, 2013.

[15] D. C. Flanagan and S. J. Livingston, "WEPP User Summary, USDA-water erosion prediction project," *Nat. Erosion Res. Lab.*, IN, USA, Tech. Rep. 11, Jul. 1995. [Online]. Available: https://www.ars.usda.gov/ARSUserFiles/50201000/WEPP/usersum.pdf, Accessed: Oct. 8, 2020.

[16] L. Wang *et al.*, "Implementation of channel-routing routines in the water erosion prediction project (WEPP) model," in *Proc. Soc. Ind. Appl. Math. Conf. Math. Ind. Challenges Front*, Oct. 2009, pp. 120–127, 2010, doi: 10.1137/1.9781611973303.14.

[17] R. P. C. Morgan *et al.*, *The European Soil Erosion Model (EUROSEM): Documentation and User Guide*, Silsoe Coll., Cranfield Univ., Cranfield, U.K., 1998.

[18] D. A. Woolhiser, R. E. Smith, and D. C. Goodrich, KINEROS, *A Kinematic Runoff And Erosion Model: Documentation and User Manual*, U.S. Dept. Agriculture, Agricultural Res. Service, Washington, DC, USA, 1990.

[19] W. G. Knisel (Ed.), "CREAMS: A field scale model for chemicals, runoff and erosion from agricultural management systems," Dept. of Agriculture, Science and Education Administration, USA, May 1980.

[20] D. B. Beasley, L. F. Huggins, and E. J. Monke, "ANSWERS: A model for watershed planning," *Trans. Amer. Soc. Agric. Eng.*, vol. 23, no. 4, pp. 938–944, 1980, doi: 10.13031/2013.34692.

[21] B. P. Wrobel, "The evolution of digital photogrammetry from analytical photogrammetry," *Photogrammetric Rec.*, vol. 13, no. 77, pp. 765–776, Apr. 1991.

[22] A. Eltner and G. Sofia, "Structure from motion photogrammetric technique," *Develop. Earth Surface Processes*, vol. 23, pp. 1–23, Mar. 2020, doi: 10.1016/B978-0-444-64177-9.00001-1.

[23] M. Cramer, "Photogrammetric Sensors," in *Encyclopedia of GIS*. Boston, MA, USA: Springer, 2008. DOI: 10.1007/978-0-387-35973-1_983.

[24] M. Pepe, L. Fregonese, and M. Scaioni, "Planning airborne photogrammetry and remote sensing missions with modern platforms and sensors," *Eur. J. Remote Sens.*, vol. 51, no. 1, pp. 412–436, 2018.

[25] H. Obanawa, "Quantitative measurement of the topographic change at overhanging sea cliff with small UAV survey system," in *Proc. Int. Geosci. Remote Sens. Symp.*, 2015, pp. 4684–4687, doi: 10.1109/IGARSS.2015.7326874.

[26] A. Stumpf, J. P. Malet, P. Allemand, M. Pierrot-Deseilligny, and G. Skupinski, "Ground-based multi-view photogrammetry for the monitoring of landslide deformation and erosion," *Geomorphology*, vol. 231, pp. 130–145, Feb. 2015, doi: 10.1016/j.geomorph.2014.10.039.

[27] S. Yang, Y. Guan, C. Zhao, C. Zhang, J. Bai, and K. Chen, "Determining the influence of catchment area on intensity of gully erosion using high-resolution aerial imagery: A 40-year case study from the Loess Plateau, northern China," *Geoderma*, vol. 347, pp. 90–102, 2019.

[28] X. B. He, K. L. Tang, and X. B. Zhang, "Soil erosion dynamics on the Chiness Loess Plateau in the last 10,000 years," *Mt. Res. Dev.*, vol. 24, no. 4, pp. 342–347, 2004.

[29] K. L. Cook, "An evaluation of the effectiveness of low-cost UAVs and structure from motion for geomorphic change detection," *Geomorphology*, vol. 278, pp. 195–208, 2017.

[30] B. Kršák *et al.*, "Use of low-cost UAV photogrammetry to analyze the accuracy of a digital elevation model in a case study," *Measurement*, vol. 91, pp. 276–287, 2016.

[31] P. N. Jayson-Quashigah, K. A. Addo, B. Amisigo, and G. Wiafe, "Assessment of short-term beach sediment change in the volta delta coast in ghana using data from unmanned aerial vehicles (drone)," *Ocean Coastal Manage.*, vol. 182, , 2019, Art. no. 104952.

[32] A. Eltner, D. Schneider, and H. G. Maas, "Integrated processing of high resolution topographic data for soil erosion assessment considering data acquisition schemes and surface properties," in *Proc. Int. Archives Photogrammetry, Remote Sens. Spatial Inf. Sci.*, 2016, pp. 813–819, doi: 10.5194/isprsarchives-XLI-B5-813-2016.

[33] P. Hänsel, M. Schindewolf, A. Eltner, A. Kaiser, and J. Schmidt, "Feasibility of high-resolution soil erosion measurements by means of rainfall simulations and SfM photogrammetry," *Hydrology*, vol. 3, no. 4, pp. 1–16, 2016.

[34] D. H. Rieke-Zapp and M. A. Nearing, "Digital close range photogrammetry for measurement of soil erosion," *Photogrammetric Rec.*, vol. 20, no. 109, pp. 69–87, 2005.

[35] M. Balaguer-Puig, Á. Marqués-Mateu, J. L. Lerma, and S. Ibáñez-Asensio, "Quantifying small-magnitude soil erosion: Geomorphic change detection at plot scale," *Land Degradation Develop.*, vol. 29, no. 3, pp. 825–834, 2018.

[36] M. Balaguer-Puig, "Empirical analysis of photogrammetric solutions in soil erosion studies in the laboratory," (in Spanish), Ph.D. dissertation, Univ. Valencia, Valencia, Spain, 2015.

[37] N. D. Cullen, A. K. Verma, and M. C. Bourke, "A comparison of structure from motion photogrammetry and the traversing micro-erosion meter for measuring erosion on shore platforms," *Earth Surf. Dyn.*, vol. 6, no. 4, pp. 1023–1039, 2018.

[38] M. R. James, S. Robson, and M. W. Smith, "3-D uncertainty-based topographic change detection with structure-from-motion photogrammetry: Precision maps for ground control and directly georeferenced surveys," *Earth Surface Processes Landforms*, vol. 42, no. 12, pp. 1769–1788, 2017, doi: 10.1002/esp.4125.

[39] G. Soares, L. Campos-Inocencio, M. R. Veronez, L. G. da Silveira, F. Bordin, and F. P. Marson, "Analysis of positional and geometric accuracy of objects in survey with unmanned aerial vehicles (UAV)," in *Proc. IEEE Int. Symp. Geosci. Remote Sens.*, Valencia, Spain, Jul. 22–27, 2018, pp. 5693–5696, doi: 10.1109/IGARSS.2018.8517315.

[40] F. Agüera-Vega *et al.*, "Reconstruction of extreme topography from UAV structure from motion photogrammetry," *Measurement*, vol. 121, pp. 127–138, 2018, doi: 10.1016/j.measurement.2018.02.062.

[41] M. Röder, S. Hill, and H. Latifi, "Best practice tutorial: Technical handling of the UAV 'DJI Phantom 3 Professional' and processing of the acquired data," Univ. Würzburg, Würzburg, Germany, Tech. Rep., Apr. 2017, doi: 10.13140/RG.2.2.36355.91680.

[42] Regionalization and Cadastre Office, "The CR05 Reference System and the Transverse Mercator Projection for Costa Rica CRTM05," (in Spanish), Costa Rica, National Geographic Institute, 2009.

[43] R. Williams, "DEMs of difference," *Geomorphological Techn.*, vol. 2, pp. 1–17, 2012.

[44] J. Singh, H. V. Knapp, and M. Demissie, "Hydrologic modeling of the iroquois river watershed using HSPF and SWAT," *Journal of the American Water Resources Association JAWRA*, No. 04030, Apr. 2005, doi: 10.1111/j.1752-1688.2005.tb03740.x.

[45] D. N. Moriasi, J. G. Arnold, M. W. Van Liew, R. L. Bingner, R. D. Harmel, and T. L. Veith, "Model evaluation guidelines for systematic quantification of accuracy in watershed simulations," *Trans. ASABE*, vol. 50, no. 3, pp. 885–900, 2007, doi: 10.13031/2013.23153.

[46] M. Mendez, B. Maathuis, D. Hein-Griggs, and L. F. Alvarado-Gamboa, "Performance evaluation of bias correction methods for climate change monthly precipitation projections over Costa Rica," *Water (Switzerland)*, vol. 12, no. 2, 2020, Art. no. 482, doi: 10.3390/w12020482.

[47] J. Solano and R. Villalobos, "Climate Regions and Subregions of Costa Rica," (in Spanish), *Costa Rica: Instituto Metereológico Nacional*, 2005. [Online]. Available: https://www.imn.ac.cr/documents/10179/20909/Regionalización+climática+de+Costa+Rica, Accessed: Aug. 21, 2020.

[48] G. W. Gee and D. Or, "Particle size analysis," in *Methods of Soil Analysis*, J. H. Dane and G. C. Topp, Eds. Madison, WI, USA: Soils Sci. Soc. Amer., 2002, pp. 255–294.
[49] H. P. Blume *et al.*, *Scheffer/Schachtschabel: Textbook of Soil Science*, Heidelberg, Germany: Spektrum Akademischer Verlag, (in German), 2010.
[50] FAO, Rome, Italy, "Soil tillage in Africa: Needs and challenges," FAO Soils Bull., 1993.
[51] J. Wang, Q. He, P. Zhou, and Q. Gong, "Test of the RUSLE and key influencing factors using GIS and probability methods: A case study in nanling national nature reserve, South China," *Adv. Civ. Eng.*, vol. 2019, 2019, Art. no. 7129639, doi: 10.1155/2019/7129639.
[52] R. S. S. Amorim, D. D. Da Silva, F. F. Pruski, and A. T. De Matos, "Performance evaluation of the water erosion prediction models USLE, RUSLE and WEPP for different edaphoclimatic conditions in Brazil, (In Portuguese)," *Engenharaia Agrícola*, (In Portuguese), vol. 30, no. 6, pp. 1046–1049, 2010, doi: 10.1590/S0100-69162010000600006.
[53] N. Efthimiou, "Performance of the RUSLE in mediterranean mountainous catchments," *Environ. Process.*, vol. 3, pp. 1001–1019, 2016, doi: 10.1007/s40710-016-0174-y.
[54] D. J. Brus and J. J. H. Van Den Akker, "How serious a problem is subsoil compaction in the Netherlands? A survey based on probability sampling," *Soil*, vol. 4, pp. 37–45, 2018, doi: 10.5194/soil-4-37-2018.
[55] S. Arriola-Valverde, K. Villagra-Mendoza, M. Méndez-Morales, N. Gómez-Calderón, M. Solórzano-Quintana, and R. Rimolo-Donadio, "Analysis of crop dynamics through close-range UAS photogrammetry," in *Proc. IEEE Int. Symp. Circuits Syst.: FoodCAS Track*, Seville, Spain, Oct. 12–14, 2020, pp. 1–5, doi: 10.1109/ISCAS45731.2020.9181285.

Sergio Arriola-Valverde (Student Member, IEEE) received the Lic. degree in electronics engineering and the M.Sc. degree in embedded systems from the Instituto Tecnológico de Costa Rica (ITCR), Cartago, Costa Rica, in 2015 and 2018, respectively. He is currently working toward the Ph.D. degree with ITCR, working on the topic of remote sensing and electrical communications.

Since 2015, he has been with the Electronics Engineering Department, ITCR, as a Lecturer. His research interests include remote sensing, close-range UAS photogrammetry, embedded systems, electrical communications, and data science analysis and image analysis with artificial intelligence techniques.

Luis Carlos Villalobos-Avellán has been working toward the graduate degree in the Agricultural Engineering Program, Instituto Tecnológico de Costa Rica (ITCR), Cartago, Costa Rica, since 2016.

Since 2017, he has been working as a Student Research Assistant with the Agricultural Engineering Department, ITCR, and in 2019 he was awarded with a Research Grant at the Centro de Alta Tecnología (CENAT), Costa Rica. His current research interests include hydraulic modeling, georeferencing techniques, and the utilization of UAS platforms in agriculture.

Karolina Villagra-Mendoza received the B.S. degree in agricultural engineering from the Instituto Tecnológico de Costa Rica (ITCR), Cartago, Costa Rica, in 1999, the M.Sc. degree in environmental engineering, and the Ph.D. degree in engineering, both from the Technische Universität Hamburg (TUHH), Hamburg, Germany, in 2006 and 2019, respectively.

From 2006 to 2011, she was with the Institute of River and Coastal Engineering, TUHH. Since 2012, she has been a Senior Lecturer with the Agricultural Engineering Department, ITCR. Her current research interests include soil and water conservation, hydrological processes, environmental protection, soil erosion control, biochar application and production technology, and irrigation management systems.

Renato Rimolo-Donadio (Senior Member, IEEE) received the B.S. and Lic. degrees in electrical engineering from the Instituto Tecnológico de Costa Rica (ITCR), Cartago, Costa Rica, in 1999 and 2004, respectively, the M.Sc. degree in microelectronics and microsystems and the Ph.D. degree in electrical engineering from the Technische Universität Hamburg (TUHH), Hamburg, Germany, in 2006 and 2010, respectively.

From 2006 to 2012, he was with the Institute of Electromagnetic Theory, TUHH. From 2012 to 2014, he was with the IBM Thomas J. Watson Research Center, Yorktown Heights, NY, USA. He is currently a Full Professor with the Electronics Engineering Department, ITCR. His current research interests include the system-level modeling and optimization of interconnects, the analysis of signal and power integrity problems, high-speed integrated circuit design and remote sensing techniques.